Numerical simulation of fiber–matrix debonding: Inverse identification of interface properties

H. Girard, Aurélien Doitrand, B. Koohbor, R.G. Rinaldi, N. Godin, D. Long, J. Bikard, L. Trouillet-Fonti

Numerical simulation of fiber-matrix debonding: inverse identification of interface properties

H. Girard[a,b,*], A. Doitrand[a], B. Koohbor[c], R.G. Rinaldi[a], N. Godin[a], D. Long[a], J. Bikard[b], L. Trouillet-Fonti[b]

[a] *Univ Lyon, INSA Lyon, Université Claude Bernard Lyon 1, CNRS, MATEIS, UMR5510, 69621 Villeurbanne, France*

[b] *Axel'One (Solvay), 87 Avenue des Frères Perret, CS 70061, 69192 Saint Fons, France*

[c] *Department of Mechanical Engineering, Rowan University, 201 Mullica Hill Rd., Glassboro, NJ 08028, United States of America*

Abstract

Fiber-matrix interface debonding is studied by means of single-fiber epoxy-glass fiber specimens under transverse tensile loading. Experimental observations show abrupt debonding initiation between 67 and 83 deg. followed by stable debonding propagation. Similar abrupt debonding initiation is predicted using the coupled criterion (CC). The latter predicts crack initiation considering both stress and energy aspects from which a range of interface shear and opening critical energy release rates (ERR) and strengths can be derived. Depending on these parameters, initiation is found to be either driven by energy solely or by both stress and energy conditions. The loading required for initiation depends on the opening (mode I) critical ERR and tensile and shear strengths. The debonding arrest angle also depends on the shear (mode II) critical ERR. Consequently, a three steps methodology to identify the interface properties is described and an optimum set of parameters is determined by focusing on the stable debonding propagation after initiation using Linear Elastic Fracture Mechanics.

Keywords: Fiber-matrix debonding, Finite Fracture Mechanics, Linear Elastic Fracture Mechanics

1. Introduction

Multi-material interface problems are encountered in many industrial sectors as they often appear in assembled parts or heterogeneous materials. Additionally, structures made from these elements are nowadays increasingly employed, especially in aeronautic and aerospace applications, wherein bonded assemblies or composite materials are used primarily for weight reduction. The mechanics of such multi-material interface problems inherently span over various length scales, from the macro-scale for bonded large parts to the micro-scale for the interface of non-homogeneous material components, such as the fiber-matrix interface for long fiber composites. For the latter, the fiber-matrix interface is a key aspect of global composite mechanical properties since it

*Corresponding author

Email address: hugo.girard@insa-lyon.fr (H. Girard)

Nomenclature	
ERR	Energy Release Rate
IERR	Incremental Energy Release Rate
CC	Coupled criterion
CZM	Cohesive Zone Model
FFM	Finite Fracture Mechanics
LEFM	Linear Elastic Fracture Mechanics
ϕ	Fiber diameter
r	Fiber radius
U	Imposed displacement
σ^{∞}	Far-field tensile stress - global stress
$\sigma^{\infty}_{\text{req}}$	Far-field tensile stress required to fulfill the energy condition
θ_{d}	Debonding angle
G_{inc}	Incremental Energy Release Rate
G	Energy Release Rate
W	Elastic strain energy
σ_{nn}	Interface normal stress
τ_{nt}	Interface shear stress
σ_{c}	Interface tensile strength
τ_{c}	Interface shear strength
μ	Shear to tensile strength ratio
σ_{eq}	Equivalent stress
f	Stress criterion
G_{c}	Interface local critical energy release rate
$\overline{G_{\text{c}}}$	Interface global critical energy release rate
ψ	Mode mixity
G_{IC}	Critical energy release rate - mode I
G_{IIC}	Critical energy release rate - mode II
λ	G_{IIC} to G_{IC} ratio
θ_{ini}	Debonding angle at initiation
θ_{arrest}	Debonding angle after unstable growth
θ_{l}	Debonding angle after unstable growth - lower bound
θ_{u}	Debonding angle after unstable growth - upper bound
ν	Poisson's ratio
E	Young modulus
L_{mat}	Material characteristic length
$\theta_{\text{d}}^{\text{ini}}$	Debonding angle after unstable growth - lower bound
$\theta_{\text{d}}^{\text{stop}}$	Debonding angle fully debonded
$\sigma^{\infty}_{\text{sim}}$	Numerical far-field tensile stress
$\sigma^{\infty}_{\text{exp}}$	Experimental far-field tensile stress

drives damage initiation and load transfer [1, 2, 3, 4]. In fact, fiber-matrix interface debonding is usually the first type of damage that occurs in long fiber composites subjected to transverse loading. After initiation, the interface debonding propagates and often kinks into the matrix. This

phenomenon conducts to the coalescence of debonded interfaces and their associated kinked-out matrix microcracks, leading to complete failure of the composite lamina. [5]. It can then result in the delamination between plies, fibers breakage, or , in severe cases, to the complete failure of a composite part. Thus, the fiber-matrix interface has a strong influence on the damage sequence in the composite so that it is crucial to characterize the fiber-matrix interface in order to prevent or control the damage in composites.

Many experimental methods are currently used to characterize interface fracture properties. Herrera-Franco and Drzal [6] and Zhandarov and Mader [7] reviewed most of the methods for measuring the fiber-matrix interface strength. The following methods can be used for interfacial shear strength determination: pull-out test [8], microbonding test [8], single fiber fragmentation test [9], micro-indentation test [10]. It has been shown that a large variability exists between the properties measured by all the aforementioned approaches [6]. Moreover, analytical models are mainly employed for interface property determination [11] without carefully accounting for the real specimen geometry and loading.

Fiber-matrix debonding in specimens subjected to transverse loading occurs first in opening mode, the interface being then locally loaded under combined shear and opening stresses. Nevertheless, most of the reported approaches focus on shear properties. Other experimental approaches have been developed, such as the Broutman test on a single fiber [12, 13]. The latter uses a global compressive load that leads to a local tensile load at the fiber-matrix interface thanks to an adequate sample geometry. Gundel *et al.* [14] elaborated a cruciform shape sample to avoid free edge stress fields perturbation. This method allows transverse interface characterization under tensile loading [15, 16]. Nevertheless, these tests do not provide precise crack sizes and are mainly limited to transparent matrices to allow optical observation of the fiber.

Therefore, new experimental approaches have recently emerged to directly observe the debonding stages at the sample free edges. Some authors [17, 18] employed an approach based on a single glass fiber embedded in an epoxy sample subjected to transverse uniaxial tensile loading. Coupling *in situ* interface observation and numerical simulation showed stages of damage from tensile to shear dominated crack propagation. Debonding initiated at the free edge due to stress perturbation and propagated along the fiber towards the specimen center. Montgomery *et al.* [19] developed micro-scale digital image correlation (DIC) approach to observe crack initiation and propagation at the free edge thanks to a multi-layered DIC pattern. These methods allowed direct measurement of the size of the debonding at the free edges and thus, coupled with numerical simulation, enabled characterization of the interface properties. Nevertheless, these studies have focused on small diameter fibers, *e.g.* few microns, where debonding remains difficult to observe optically.

To address this scaling issue, Livingston and Koohbor [20] recently performed an experimental observation of macro-scale debonding. Composite specimens were tested under uniaxial tension and full-field measurements at the fiber vicinity was performed to observe debonding stages. For this purpose, DIC was used to extract local strain fields and debonding angle at the free edges as a function of applied load.

From a numerical point of view, the debonding of a single cylindrical inclusion under transverse loading has been studied based on Cohesive Zone Model (CZM) [21, 22, 23], Finite Fracture Mechanics (FFM) [24, 25, 26] or Linear Elastic Fracture Mechanics (LEFM) [27, 28]. FFM is numerically efficient in predicting crack initiation but can also assess crack propagation [29, 30] and reverts to LEFM when infinitesimal crack increments are considered. CZM is more computationally expensive but describes both crack initiation and propagation. Mantič [31] first addressed

debonding initiation using the coupled criterion (CC) introduced by Leguillon [32], which predicts both the initiation loading and debonding angle. Nevertheless, these studies are exclusively based on numerical aspects and lack experimental verification.

This work aims at validating FFM and LEFM predictions with experimental characterization of debonding initiation and propagation in order to identify the properties of the fiber-matrix interface. This approach opens identification possibilities by considering simultaneously the opening and shear modes. Moreover, the identified properties are based on two distinct phenomena (initiation and propagation of debonding), which allows an accurate identification. Experimental characterization of fiber-matrix debonding is detailed in Section 2. Debonding initiation and propagation is addressed using FFM and LEFM in Section 3, to capture all stages of debonding. Finally, a three steps methodology allowing the identification of the interface properties is presented in Section 4.

2. Experiments

2.1. Sample preparation and mechanical testing

Composite specimens were manufactured by embedding a 2 mm diameter glass macro-fiber in a thermoset epoxy resin whose isotropic elastic properties are given in Table 1. Epoxy resin mixture was then poured into the mold and cured for 48 hours at room temperature. Samples were finally polished and patterned for DIC measurements. Uniaxial tensile tests at a constant crosshead speed of 5 mm/min were performed. A camera was used to capture the debonding steps *in situ* using a high-magnification macro lens. The camera recording was synchronized with the load cell for a similar extraction time. This approach allowed DIC measurements of the displacement fields from which strain fields are derived.

Property	Epoxy	Glass Fiber
Young Modulus [GPa]	2.36 ± 0.10	63
Poisson's ratio	0.40 ± 0.04	0.3

Table 1: Mechanical properties of the matrix [20] and fiber (obtained from the manufacturer).

A custom jig held the fiber in the center of a silicone mold, which was sized according to ASTM D638. Figure 1a details the specimen geometry and dimensions.

2.2. Experimental characterization of the debonding process

The numerical approach presented in the sequel focuses on debonding initiation and propagation. It enables the determination of debonding angle variation as a function of the applied stress for a given set of interface fracture properties. The inverse identification of these properties thus requires the measurement of the debonding angle as a function of the applied stress. Two methods were used in order to experimentally estimate the debonding angle variation as a function of the far-field tensile stress, hereafter referred to as global stress σ^{∞}. The first method consists of optical detection of the debonding. This method is performed independently by two operators to evaluate the measurement uncertainty due to, for instance, the sample pattern possibly obscuring the crack and the pattern black components that may be confused with the crack. The second method is based on DIC residuals [33]. The residuals are expected to be the largest at locations where debonding occurs since it triggers the appearance of black pixels not present on the reference image

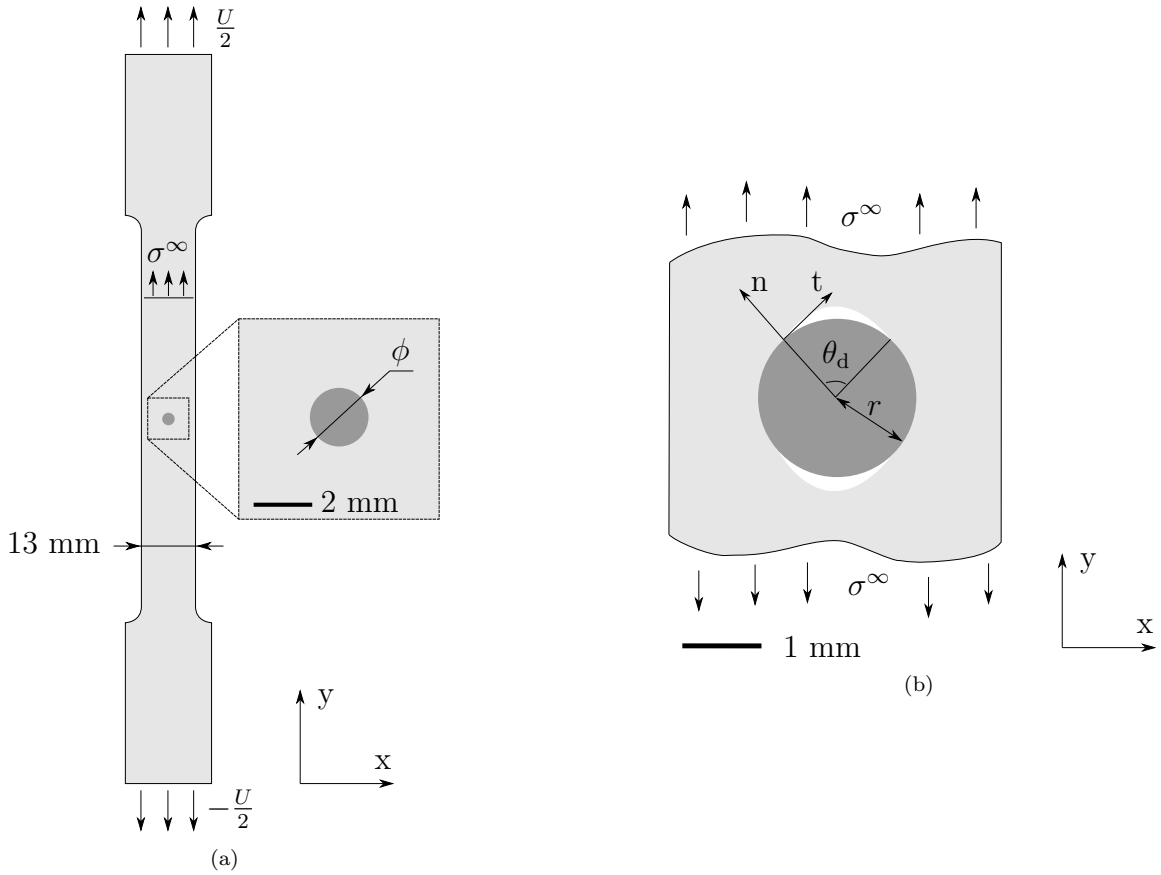

Figure 1: (a) Single-fiber specimen geometry and dimensions. (b) Schema of the single-fiber numerical model.

of the undeformed specimen. Therefore, debonding angle is estimated by applying a threshold to the residuals map. Threshold varying from 1% to 3% of the gray level dynamic are chosen so that the measured debonding angle remains zero before debonding initiation. The debonding angle (θ_d) variation as a function of the global stress (σ^∞) obtained using both approaches are shown in Figure 2.

Similar trends are obtained using both methods. The maximum difference is observed between the measurements of the two operators, mainly due to the difficulty of identifying the crack tips. Observations highlight crack initiation over a significant debonding angle for loading comprised between 3.0 MPa and 4.0 MPa, followed by a stable crack propagation phase for larger loading levels. Noticeably, the debonding angle after initiation is obtained for the same loading (*i.e.*, the same recorded image) level using both methods. Debonding angles just after initiation in the range 67 to 83 deg. are obtained (20% relative difference). Angle difference no larger than 30 degrees (21% relative difference) is obtained during the propagation phase.

3. Fiber-matrix debonding modeling

3.1. Numerical model

A 2D plane strain model under linear elasticity and small deformation assumptions is set up. A schematic representation of the model is shown in Figure 1b. The FE model geometry is bounded along (Oy) and (Ox) directions at 50 and 6.5mm, respectively, which is sufficiently large to provide

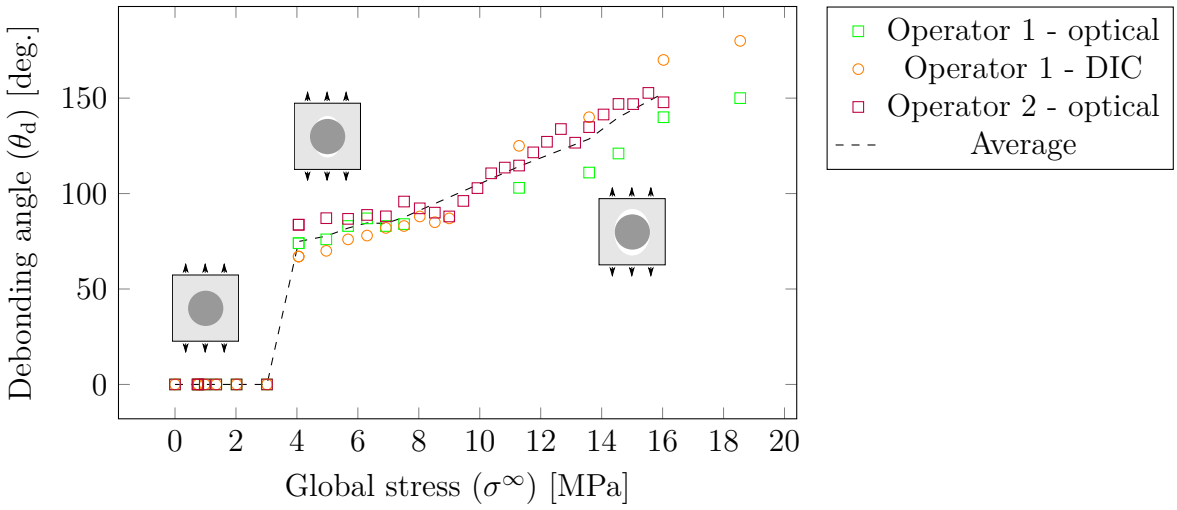

Figure 2: Variation of the debonding angle (θ_d) at one fiber pole as a function of the global stress (σ^∞) applied to the specimen.

stress fields corresponding to a remote tensile stress. Fiber-matrix interface debonding is simulated using both the CC and LEFM, which require the calculation of the stresses before debonding and the elastic energy variation as a function of the debonding angle. Livingston and Koohbor [20] experimentally observed two simultaneous debonding at both fiber poles and symmetric crack propagation. From an energy point of view, symmetric debonding leads to a slightly different amount of energy released compared to asymmetric debonding, as shown by Garcia *et al.* [24] and observed experimentally by Martyniuk *et al.* [18]. Four-node linear elements are used. The elastic properties presented in Table 1 are assigned to each component. Mesh convergence is performed in order to choose a mesh size that ensures difference on both elastic strain energy and stress no larger than 1% for a finer mesh size. In the following sections, the CC and LEFM methods are presented and applied to the simulation of debonding initiation and propagation, respectively.

3.2. Interface debonding initiation

Interface debonding initiation is studied using the CC [32]. The methodology is similar to Mantič's approach [31]. The CC predicts crack initiation by combining two conditions: sufficiently high stress field along the crack path before initiation and sufficient energy released by the crack opening (Equation (1)). Conditions that satisfy the CC form a two-equations system whose solution provides the loading and crack size at initiation and both conditions presented in Equation (1) must be satisfied to make initiation possible.

$$\begin{cases} f(\underline{\sigma}(\theta_d, \sigma^\infty), \sigma_c, \tau_c) \geq 1, \\ G_{inc}(\theta_d, \sigma^\infty) \geq \overline{G_c}. \end{cases} \tag{1}$$

The stress criterion at the interface, denoted by f, either corresponds to a tensile or polynomial criterion, see Section 3.2.1. G_{inc} represents the incremental energy release rate (IERR), that depends on the fiber radius r, obtained from the elastic strain energy (W) variation per unit thickness of the model (Equation (2)). The global interface critical energy release rate is denoted $\overline{G_c}$, which depends on the debonding angle (see Section 3.2.2).

$$G_{\text{inc}}(\theta_{\text{d}}, \sigma^{\infty}) = \frac{W(0, \sigma^{\infty}) - W(\theta_{\text{d}}, \sigma^{\infty})}{r\theta_{\text{d}}} \tag{2}$$

3.2.1. Stress condition - tensile or polynomial stress criterion?

The first condition involved in the CC depends on the stress field at the fiber-matrix interface. Several criteria exist, from a normal stress criterion (Equation (3)), to a polynomial criterion (Equation (4)), involving both normal and shear stress tensor components.

$$\frac{\sigma_{\text{nn}}}{\sigma_{\text{c}}} \geq 1 \tag{3}$$

$$\sqrt{\left(\frac{\sigma_{\text{nn}}}{\sigma_{\text{c}}}\right)^2 + \left(\frac{\tau_{\text{nt}}}{\tau_{\text{c}}}\right)^2} \geq 1 \tag{4}$$

The influence of a shear stress component superimposed onto the normal component has been evaluated in this work. Interface parameters σ_{c} and τ_{c} correspond to the interface tensile and shear strengths respectively. Figure 3a shows the influence of considering the shear component on the equivalent stress variation as a function of debonding angle for several $\mu = \tau_{\text{c}}/\sigma_{\text{c}}$, shear to tensile strength ratios, similar to those reported by Martin *et al.* [21] and Doitrand *et al.* [34]. An equivalent stress can therefore be defined, including the latter parameter (Equation (5)).

$$\sigma_{\text{eq}} = \sqrt{\sigma_{\text{nn}}^2 + \frac{1}{\mu^2}\tau_{\text{nt}}^2} \geq \sigma_{\text{c}} \tag{5}$$

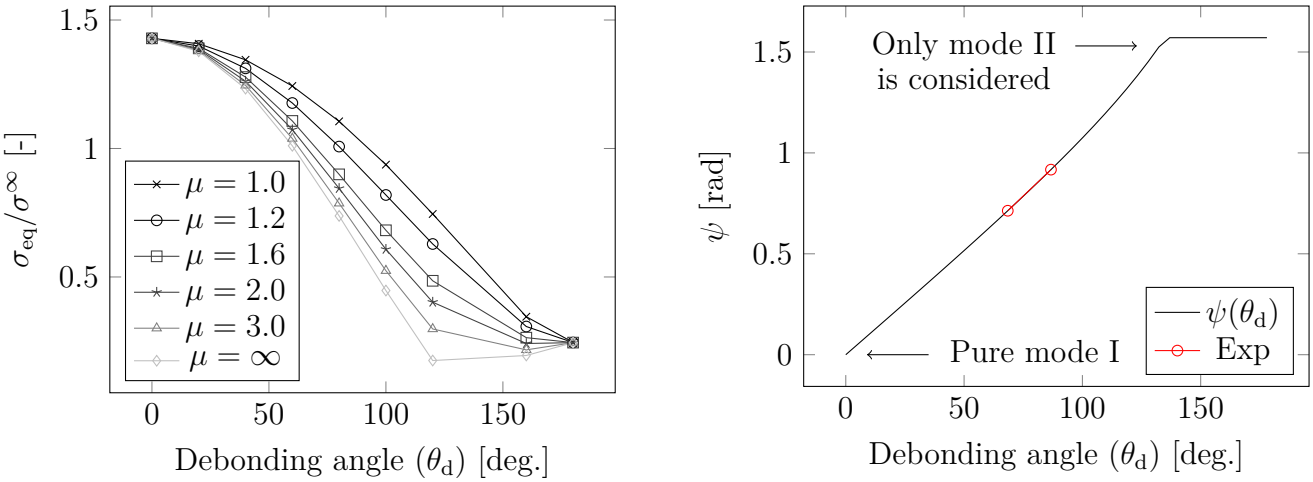

Figure 3: (a) Equivalent to global stress ratio as a function of the debonding angle for a fixed loading. (b) Mode mixity variation as a function of the debonding angle, highlighting the mode mixity range corresponding to the experimentally-measured initiation debonding angles.

Two configurations can be encountered by varying the interface properties:

- Tensile-stress induced debonding initiation: the equivalent stress reaches a local peak located at both fiber upper and lower poles;

- Shear-stress induced debonding initiation: the equivalent stress reaches two local peaks per pole, symmetrically with respect to the Oy direction.

A lower limit can therefore be set at μ to match the experimentally observed single debonding site. The minimum acceptable value of μ is 0.75 in order to maintain a monotonic decrease in equivalent stress from the single local peak. Therefore, for higher μ, the $\sigma_{\text{eq}}/\sigma^{\infty}$ ratio exhibit a monotonic decrease with increasing debonding angle. The normal stress criterion can be associated with the results obtained using $\mu = \infty$. For the same applied loading, the use of the polynomial criterion leads to a higher debonding angle on which the stress criterion is fulfilled. The higher the shear to tensile strength ratio (μ), the closer to the normal stress criterion the result is. For debonding angles larger than 140 degrees, the interface experiences shear and compressive stresses. Therefore, it is not likely that debonding initiation occurs for angles larger than 140 degrees. For the sake of simplicity, only mode II is considered above this angle and compressive stress is thus neglected in this zone. This explains the condition introduced in Equation (6) for $\sigma_{\text{nn}}(\theta_{\text{d}}) < 0$.

$$\psi(\theta_{\text{d}}) = \begin{cases} \arctan\left(\frac{|\tau_{\text{nt}}(\theta_{\text{d}})|}{\sigma_{\text{nn}}(\theta_{\text{d}})}\right), & \text{if } \sigma_{\text{nn}}(\theta_{\text{d}}) \geq 0 \\ \frac{\pi}{2}. & \text{if } \sigma_{\text{nn}}(\theta_{\text{d}}) < 0 \end{cases} \tag{6}$$

The mode mixity parameter ψ defines the proportion of shear to normal stress ratio. A condition has been applied on ψ if compressive stress is detected to consider only shear, see Equation (6). Figure 3b exhibits the mode mixity variation along the fiber-matrix interface. It shows that the interface experiences pure tensile stress at the pole parallel to the loading direction and shear combined to compressive stress, at the two lateral poles. The debonding angle measured just after initiation lies between 67 and 83 degrees. In this angle range, as seen in Figure 3b, the influence of shear stress is not negligible, which justifies the use of the polynomial criterion in the sequel. The equivalent stress σ_{eq}, introduced in Equation (5), before initiation, must be larger than the tensile strength along the area on which the debonding initiates to satisfy the stress criterion.

3.2.2. Energy condition

The second condition involved in the coupled criterion for crack initiation prediction compares the IERR to the interface critical ERR (Equation (2) and Equation (7)). The local critical energy release rate $G_{\text{c}}(\psi)$ accounts for the local mode mixity such that it varies from G_{IC} under pure opening mode to G_{IIC} under pure shear mode (Equation (8)) [35]. The global interface critical ERR, $\overline{G_{\text{c}}}$, corresponds to the average of the local interface critical ERR over the initiation crack path (Equation (7)). The local mode mixity is calculated at an angle of 0.3 deg. from the crack tip for a given debonding angle θ_{d}. The critical ERR (Equation 8), G_{c}, depends on the parameter λ which defines the ratio between G_{IIC} and G_{IC}. For instance, $\lambda = 1$ corresponds to $G_{\text{IIC}} = G_{\text{IC}}$ and $\lambda < 1$ corresponds to $G_{\text{IIC}} > G_{\text{IC}}$.

$$\overline{G_{\text{c}}} = \frac{1}{\theta_{\text{d}}} \int_0^{\theta_{\text{d}}} G_{\text{c}}(\psi(\theta_{\text{d}}))d\theta_{\text{d}} \tag{7}$$

$$G_{\text{c}}(\psi(\theta_{\text{d}})) = G_{\text{IC}}\left[1 + \tan^2\left[(1-\lambda)\,\psi(\theta_{\text{d}})\right]\right] \tag{8}$$

Figure 4a shows the IERR to critical ERR ratio and Figure 4b shows required loading ($\sigma^{\infty}_{\text{req}}$), *i.e.* to fulfill the energy criterion, to applied loading (σ^{∞}) ratio as a function of the debonding angle for various values of λ.

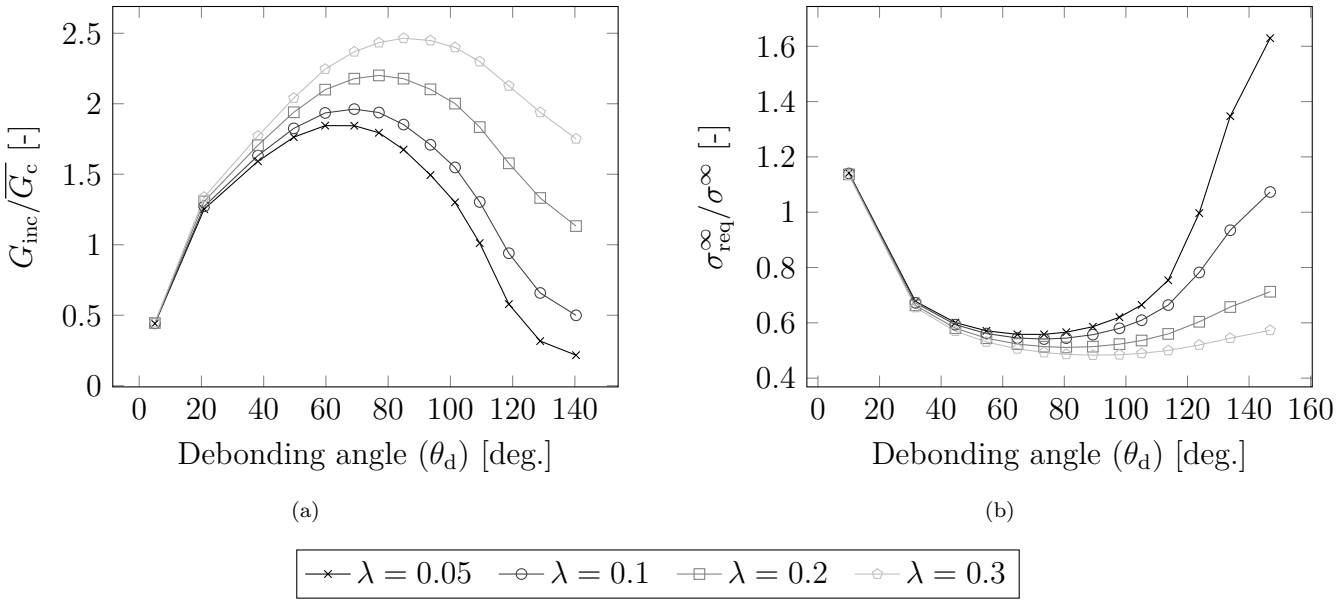

Figure 4: (a) Incremental to critical ERR ratio and (b) normalized required stress to fulfill the energy criterion variations as a function of the debonding angle, for various $G_{\text{IC}}/G_{\text{IIC}}$ ratio.

Each curve exhibits similar trends: for a small crack angle, a small amount of elastic strain energy is released which corresponds to a large imposed stress to fulfill the energy criterion. Therefore, there exists an optimal angle which maximizes the incremental ERR to critical ERR ratio and, therefore, minimizes the imposed stress to fulfill the energy criterion.

3.2.3. Coupled stress and energy criteria

The CC consists of determining the minimum loading and corresponding debonding angle θ_{ini} for which the stress and the energy conditions are simultaneously fulfilled. The equivalent stress decreases monotonically whereas the incremental to critical ERR ratio exhibits a maximum. Therefore, two scenarios can be identified:

- Scenario 1 (Figure 5a) - stress and energy driven configuration: when the intersection point of the two curves corresponds to an angle smaller than that corresponding to the maximum of the incremental to critical ERR, the favorable configuration corresponds to the intersection of the two curves;
- Scenario 2 (Figure 5b) - energy-driven configuration: when the intersection point of the two curves corresponds to an angle greater than that corresponding to the maximum of the incremental to critical ERR, the favorable configuration is therefore the angle maximizing the IERR to critical ERR ratio.

3.3. Interface debonding propagation

Once interface debonding initiates, LEFM can be applied to assess its propagation. The condition for interface debonding propagation states that the ERR must exceed the local critical energy release rate, see Equation (9).

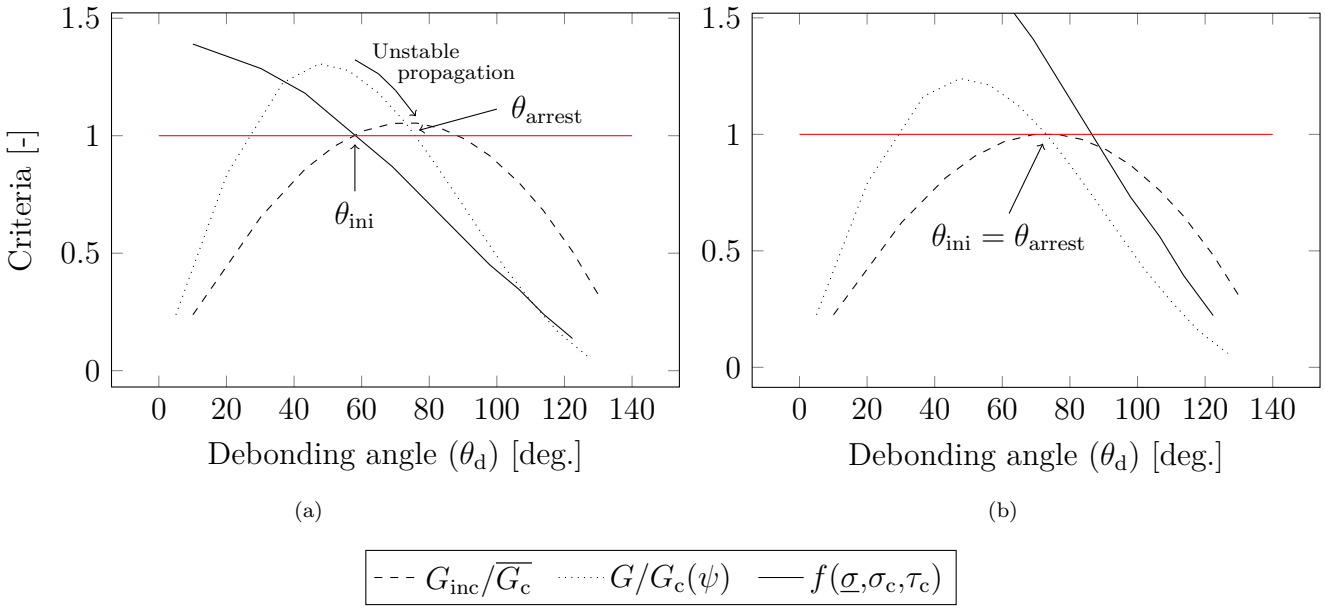

Figure 5: Criteria for IERR to critical ERR ratio and ERR to critical ERR variation as a function of the debonding angle for both scenario 1 (a) and scenario 2 (b).

$$G \geq G_{\text{c}}(\psi) \tag{9}$$

Experimental observations show a stable crack propagation phase after initiation, see Figure 2. For scenario 2, the crack remains stable just after initiation, because $G_{\text{inc}} = G = G_{\text{c}}$ at debonding initiation. Conversely, for scenario 1, $G > G_{\text{c}}$ at initiation therefore the debonding propagates in an unstable manner until $G < G_{\text{c}}$.

Considering the limitations associated with the image-based experimental basis of this work [20], an accurate assessment of the unstable crack propagation step was impossible. In particular, the image acquisition rate ,*i.e.*, one frame per second, utilized in the experiments is not fast enough to provide any meaningful information regarding the unstable propagation step. As such, interface appears to remain undamaged until a finite crack increment. This observation can be attributed to the direct stable crack, *i.e.*, scenario 2, or to the end of the unstable crack propagation, as described in scenario 1.

The ERR is evaluated numerically as the opposite of the elastic strain energy derivative with respect to the debonding surface, obtained by successively unbuttoning the nodes along the interface. The normalized equivalent stress, IERR and ERR variations as a function of debonding angle obtained for the debonding initiation loading are shown for both scenarios in Figure 5. Figure 5a shows a configuration where crack initiation is triggered by both stress and energy conditions. θ_{ini} corresponds to the initiation debonding angle. At debonding initiation, $G(\theta_{\text{ini}}) > G_{\text{c}}(\theta_{\text{ini}})$, there is an unstable propagation of the debonding until a debonding angle θ_{arrest} verifying $G(\theta_{\text{arrest}}) < G_{\text{c}}(\theta_{\text{arrest}})$. Since no increase in the loading is necessary so that the debonding propagates up to θ_{arrest}, the unstable propagation following initiation is expected to occur simultaneously. Therefore, the debonding angle measured experimentally can be compared to θ_{arrest} rather than to θ_{ini}. Figure 5b shows a configuration where crack initiation is driven by the energy condition. The initiation debonding angle corresponds to the maximum of the normalized

IERR, which verifies $G(\theta_{\text{ini}}) = G_{\text{c}}$ and $\mathrm{d}G/\mathrm{d}\theta_{\text{d}}(\theta_{\text{ini}}) < 0$. Therefore, the initiation debonding angle is also an arrest angle in this configuration so that $\theta_{\text{arrest}} = \theta_{\text{ini}}$.

3.4. Unstable propagation? Identification of the finite crack length

The approach to identify the arrest angle led to the identification of the debonding angle lower limit denoted θ_{l} on Figure 6a.

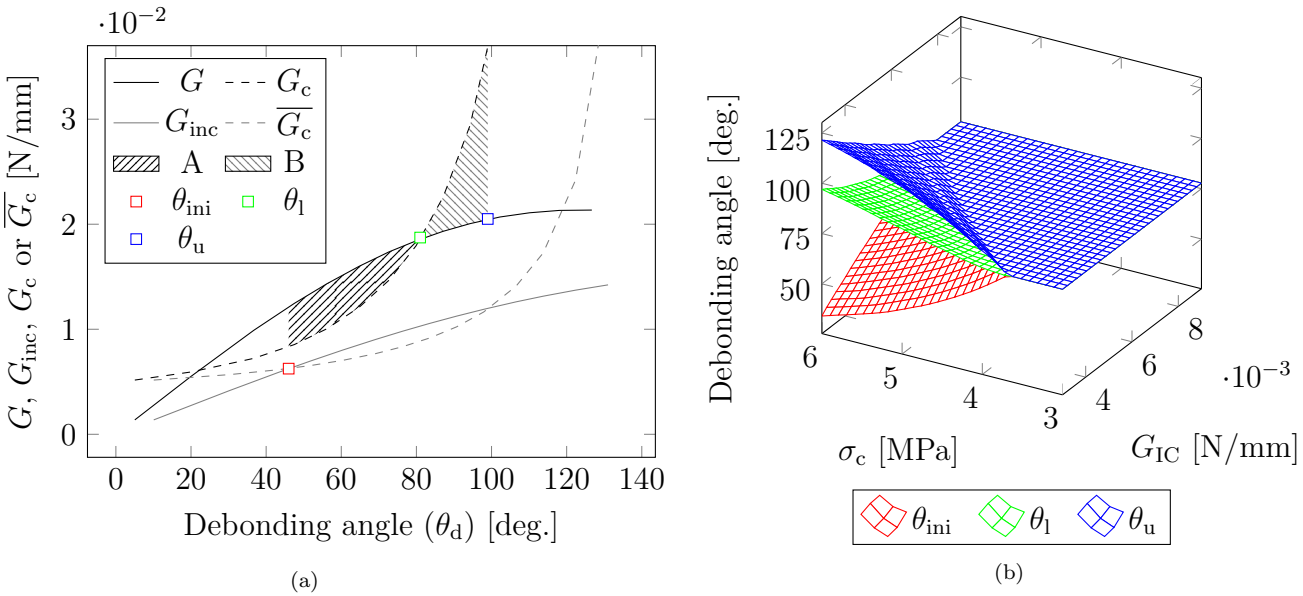

Figure 6: (a) Variation of G, G_{inc}, G_{c} and $\overline{G_{\text{c}}}$ as a function of the debonding angle for a loading leading to crack initiation. (b) Variation of the initiation angles as a function of the interface properties for $\tau_{\text{c}} = 1.2\sigma_{\text{c}}$ and $\lambda = 0.2$.

However, during the unstable propagation phase from θ_{ini} to θ_{l}, there is an excess energy ($G > G_{\text{c}}$) that has not been consumed for crack propagation (hatched zone A in Figure 6a). This excess energy may be consumed by further propagation of the crack, which enables defining an upper bound for the arrest angle, θ_{u}. This upper bound actually verifies that A and B areas (Figure 6a) are identical.

Figure 6b shows the initiation (θ_{ini}) debonding angle as well as lower (θ_{l}) and upper (θ_{u}) bounds for the arrest debonding angle obtained for several interface property couples. These curves are confounded for sufficiently small tensile strengths or sufficiently large critical ERR, corresponding to configurations driven only by the energy criterion. However, configurations driven by both stress and energy conditions are retrieved for large enough tensile strengths and small enough critical ERR, result in different lower and upper bounds of the debonding angle.

The differences between the initiation and arrest angles are larger for either larger tensile strengths or smaller critical ERR. Increasing σ_c or decreasing G_{c} actually result in decreasing the material characteristic length $\ell_{\text{mat}} = EG_c/((1-\nu^2)\sigma_{\text{c}}^2)$. Since the debonding angle obtained using the CC is a fraction of the material characteristic length [36, 37, 38], it explains that a decrease in the material characteristic length results in a decrease in the initiation angle and an increase in the arrest angle. Larger debonding arrest angles are finally obtained in configurations driven by both conditions rather than in configurations driven only by the energy condition.

4. Inverse identification of the interface properties

The inverse identification procedure is based on the following strategy:

1. Identification of a range of σ_c, τ_c, G_{IC} and G_{IIC} leading to a crack initiation stress (σ^∞) consistent with experimental observations;
2. Definition of a range of σ_c, τ_c, G_{IC} and G_{IIC} leading to a debonding arrest (θ_{arrest}) close to that found experimentally;
3. Definition of a range of G_{IC} and G_{IIC} leading to crack propagation stress (σ^∞) and angles (θ_d) similar to those found experimentally.

The three steps are fully described in the upcoming subsections.

4.1. Properties identification based on crack initiation

According to experimental measurements, the global stress corresponding to crack initiation is comprised between 3.02 and 4.05 MPa (see Section 2.2). Because of linear elasticity and small deformation assumptions, the interface properties can be varied simply during the post-processing step of the FE calculations, which makes the interface property determination computationally efficient. Figure 7a shows set of interface properties identified for $\sigma^\infty = 4.05$ MPa for $\lambda = 0.22$.

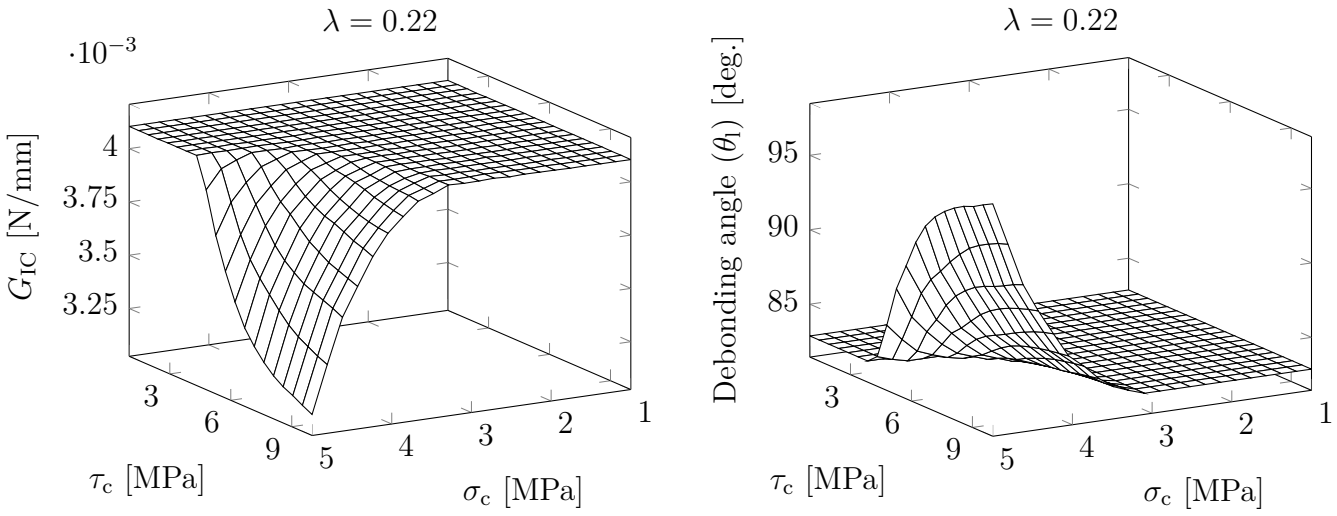

Figure 7: (a) Description of the interface parameters leading to a crack initiation at a global stress applied of 4.05 MPa and the corresponding arrest debonding (b). The parameter λ is set to 0.22 as an example.

For sufficiently small tensile or shear strengths, a constant G_{IC} is identified. This is related to configurations driven only by the energy criterion. In such configurations, the stress criterion is already fulfilled and crack initiation depends only on the normalized IERR maximum. However, configurations driven by both stress and energy conditions are encountered for sufficiently large tensile and shear strengths, which results in the decrease of G_{IC} with increasing shear or tensile strength. The debonding arrest angle variation is related to G_{IC} variation (Figure 7b). For configurations driven only by the energy condition, *i.e.*, corresponding to the G_{IC} plateau, a constant debonding angle corresponding to the normalized IERR maximum is obtained. For

interface properties corresponding to a smaller G_{IC}, the debonding angle is larger than the value at the plateau.

The second step of the identification procedure consists in restricting the obtained range of properties so that the arrest debonding angle corresponds to the one measured experimentally, *i.e.*, between 67 deg. and 83 deg. This angle corresponds to the lower limit of the arrest length (see Section 3.4). Figure 9 shows the debonding arrest angle variation as a function of the tensile and shear strengths obtained for the interface properties verifying $\sigma^{\infty} = 4.05$ MPa for various λ values.

The debonding angle at the plateau mainly depends on λ, which enables determining an upper bound ($\lambda = 0.22$) above which a too large debonding angle is obtained. Conversely, using the value 0.03 leads to the minimum acceptable value to keep the plateau within the two experimental limits. Smaller values of λ can also be obtained for large tensile and shear strengths but further result in large differences in terms of debonding angle variation as a function of applied stress. They are therefore disregarded in the following.

The application of the restriction of the debonding angle has no influence on the smallest values of λ because all the couples lie between the two boundaries, see Figure 8b. Nevertheless, increasing this parameter leads to couples outside the acceptable range, as shown by the red upper boundary in Figure 8c and Figure 8a. For these configurations, the proportion of unacceptable strength and energy parameters increases with λ. Moreover, to ensure a parameter μ greater than 0.75, additional restrictions are applied to the obtained range of σ_{c} and τ_{c}. Figures 9 and Figure 10 summarize these restrictions for the strength and energy interface properties respectively.

Increasing λ leads to decrease the range of acceptable tensile and shear strengths (Figure 9) as well as critical ERR, for which a lower bound can be determined for a given λ (Figure 10).

4.2. Further property restriction based on crack propagation

By coupling the previous two steps to the crack propagation, an additional restriction can be applied to the obtained parameters. This last step of the inverse identification approach depends only on an energy condition, so that only the energy parameters are involved. Once additional loading is required for the crack to propagate, a comparison can be made between the applied experimental loading and a simulation with fixed energy parameters. The aim is to minimize an error ($\%_{\mathrm{error}}$) between these two quantities for different angles from initiation ($\theta_{\mathrm{d}}^{\mathrm{ini}}$) to a large debonding angle ($\theta_{\mathrm{d}}^{\mathrm{stop}}$). The latter is detailed in Equation 10, where $\sigma_{\mathrm{sim}}^{\infty}$ and $\sigma_{\mathrm{exp}}^{\infty}$ denote the global stress obtained from experimentation and simulation respectively.

$$\%_{\mathrm{error}} = \left(\frac{1}{n} \sum_{\theta_{\mathrm{d}}^{\mathrm{ini}}}^{\theta_{\mathrm{d}}^{\mathrm{stop}}} \frac{\left| \sigma_{\mathrm{exp}}^{\infty}(\theta_{\mathrm{d}}) - \sigma_{\mathrm{sim}}^{\infty}(\theta_{\mathrm{d}}) \right|}{\sigma_{\mathrm{exp}}^{\infty}(\theta_{\mathrm{d}})} \right) \times 100 \tag{10}$$

The average $\%_{\mathrm{error}}$ is evaluated for a range of λ and G_{IC}, as shown in Figure 11a. The curve shows a valley where the error is minimal, with an average $\%_{\mathrm{error}}$ around 20%. Consequently, the adequate couples should be inside the valley. Coupling the previous restriction obtained in the first two steps and the results of the $\%_{\mathrm{error}}$ calculation leads to identify an adequate properties set, as shown in Figure 11b.

The pair that best meets all the restrictions is represented by the square mark and corresponds to the interface properties presented in the first row of Table 2. The final obtained properties are consistent with other glass fiber epoxy matrix interfaces (Table 3). Note that the properties

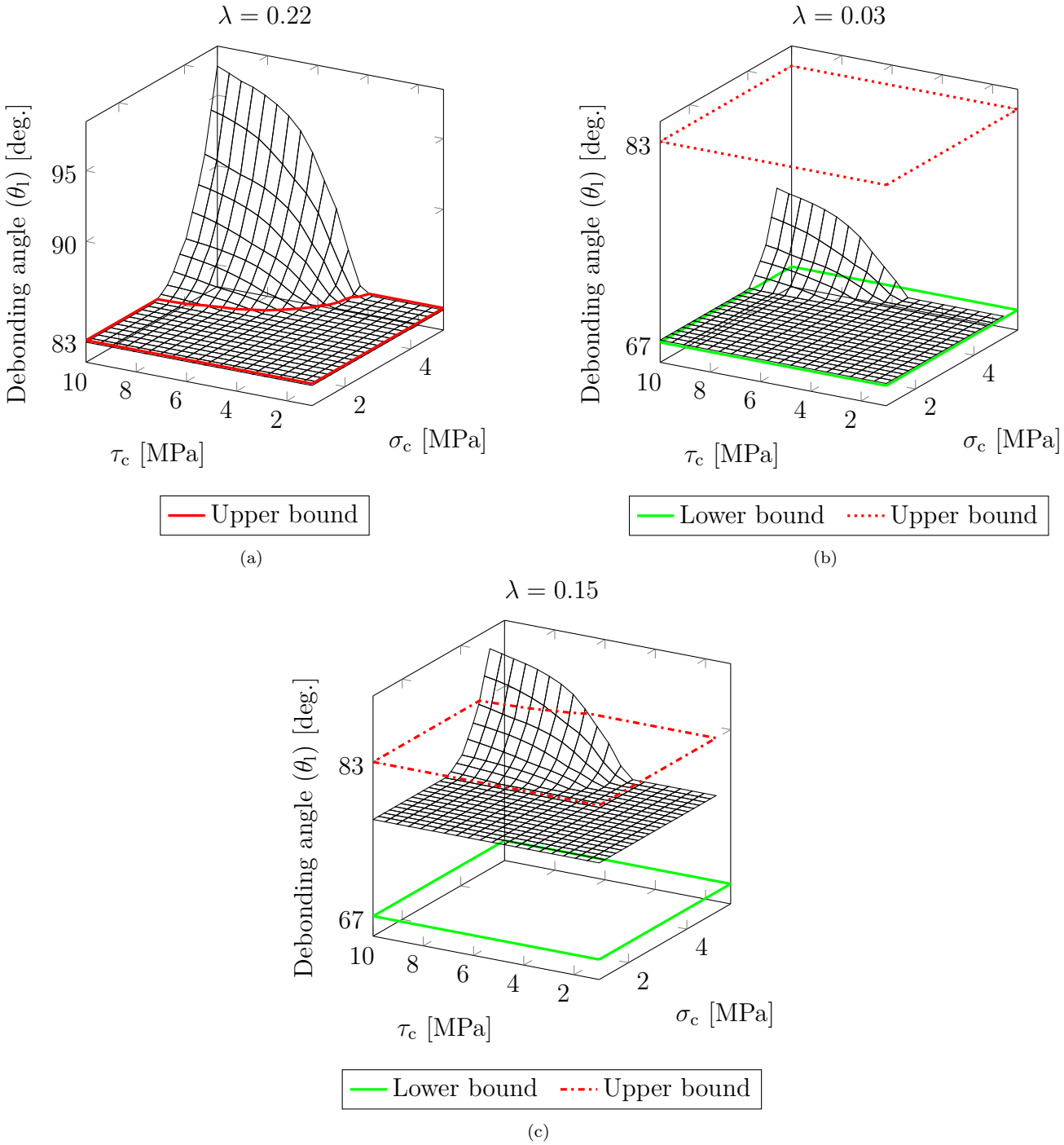

Figure 8: Variation of the lower bound of the arrest angle (θ_l) as a function of tensile and shear strengths. Couples are represented for three values of λ, (a) 0.22 (b) 0.03 (c) 0.15, with their corresponding boundaries.

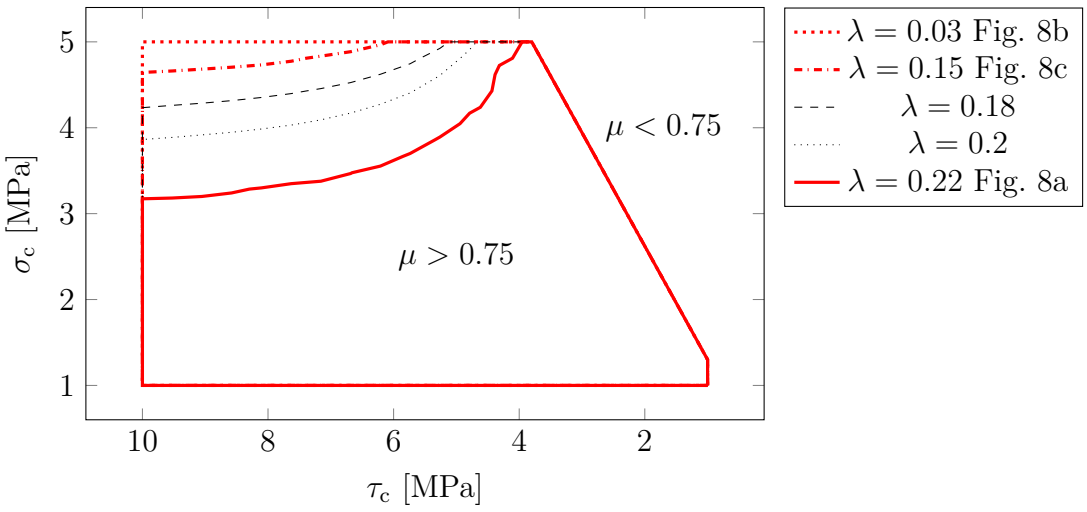

Figure 9: Stress couples restriction for several values of λ. The upper bounds depicted in red are directly related to the upper bounds of the angle restriction shown for three values of λ in Figure 8.

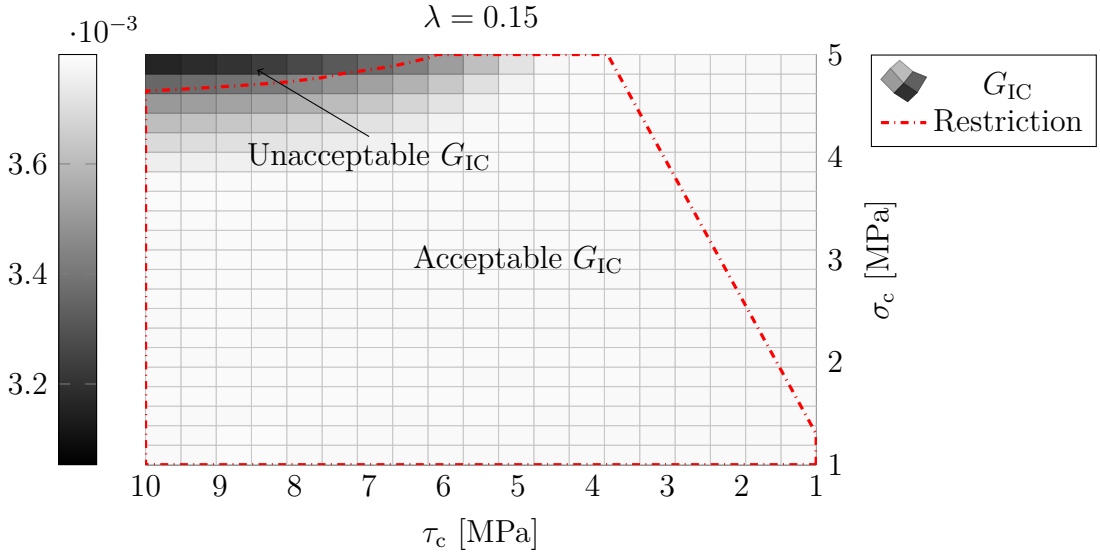

Figure 10: G_{IC} restriction for $\lambda = 0.15$. The lower bound depicted in red is directly related to the upper bound of the angle restriction shown for $\lambda = 0.15$ in the Figure 8c.

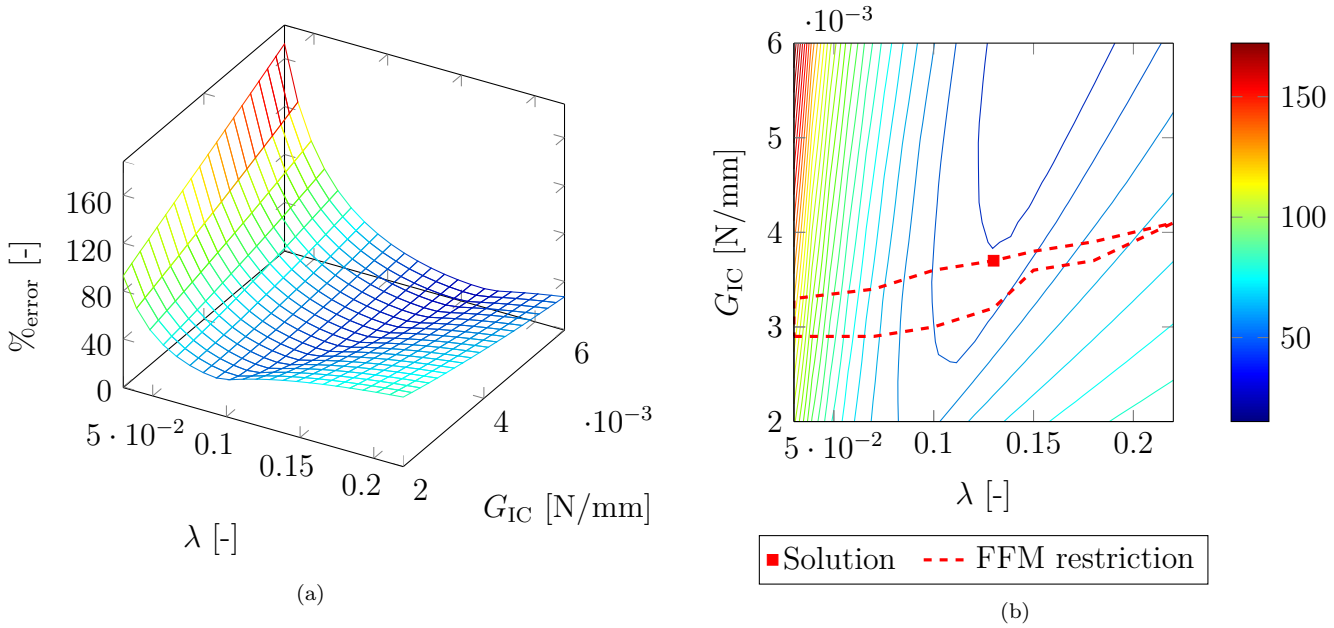

Figure 11: (a) Calculation of the $\%_{\text{error}}$ as a function of the energy parameters λ and G_{IC}. (b) Isovalues of the $\%_{\text{error}}$ with the addition of the previous restriction due to crack initiation.

presented depend strongly on the characterized interface and the method used. Thus, a direct comparison cannot be performed, nevertheless the comparison of the orders of magnitude leads to a good agreement. The debonding angle variation as a function of the applied stress are confronted in Figure 12 for the identified optimal set of parameters. The identified parameters allow capturing the initiation debonding angle and applied stress as well debonding angle propagation as a function of the applied stress for debonding angles larger than 120 deg. The debonding angle variation is slightly overestimated for intermediate angles between 90 and 120 deg. due to properties identification that mainly focuses on debonding initiation.

	G_{IC} [N/mm]	G_{IIC} [N/mm]	λ
Initiation-based, Fig. 12	0.0037	0.09	0.13
Propagation-based, Fig. 12	0.016	0.09	0.27

Table 2: Obtained interface properties.

4.3. Parameter identification based on crack propagation

Since crack initiation may be prone to some variability, for instance due to the presence of a defect, another approach can be used to identify the interface properties by first disregarding debonding initiation and focusing on propagation. This approach yields the interface properties given in the second row of Table 2.

The debonding angle variation as a function of the applied stress corresponding to these parameters is shown in Figure 12. A better description of the debonding angle variation as a function of applied stress is obtained for the propagation phase, the initiation debonding angle also being well reproduced. Nevertheless, the applied stress at debonding initiation tends to be overestimated by the latter approach.

Materials	σ_c [MPa]	τ_c [MPa]	G_{IC} [N/mm]	G_{IIC} [N/mm]	
GF[1] / Ep[2]	18 - 25	18 - 22	0.0055	0.011	[17]
GF / Ep	31				[39]
GF / Ep (NOCA)			0.002	0.006	[40]
GF / Ep	37				[41]
GF / Ep		6			[42]
GF / Ep		12			[43]
GF / Ep	10-13				[13]

[1]Glass Fiber
[2]Epoxy

Table 3: Interface properties obtained from previous works

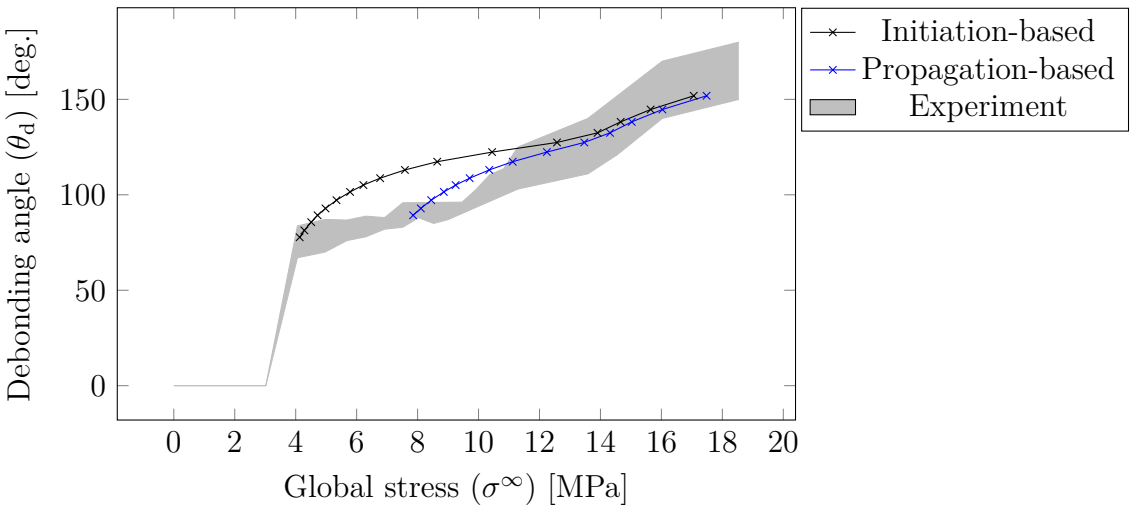

Figure 12: Variation of the debonding angle as a function of the global stress applied. Comparison between the experimental measurements and the simulation performed with the identified parameters.

4.4. Current limitations

The proposed approach enables the determination of σ_c, τ_c, G_{IC} and G_{IIC}, using a model based on a binary description of fracture considering either interface debonding or no debonding. As a consequence, we do not consider the possible presence of a process zone as in cohesive zone models, for instance. Measured debonding angle can thus account both fully damaged and process zones, whereas the above identification considers a fully damaged zone. Also, the parameter identification relies on 2D calculations whereas experimental observations are made on the specimen front surface of a flat tensile sample [20]. The stress concentration is larger at the front surface (*i.e.*, the measurement area of interest) than at the specimen center. Furthermore, the debonding initiation may not be uniform along the specimen thickness, as shown previously by the experimental observations of Martyniuk *et al.* [18]. It is expected that considering a 3D model would therefore results in slightly higher values of the identified properties which will enable comparing the results obtained considering the 3D singularity [44] or 2D plane strain or plane stress analysis [45]. It should also be noted that the properties identified depend on the choice of the stress criterion.

Finally, the proposed approach mainly depends on debonding variation as a function of the applied stress determined experimentally. This part could be improved by determining the debonding angle that minimizes the difference between simulated and experimental (obtained by DIC) displacement fields.

5. Conclusion

Experimental observations of single-fiber specimen under tensile loading evidences abrupt debonding initiation over angles in the range 67-83 deg., followed by stable debonding propagation. The observed abrupt debonding over a finite angle is predicted by the coupled criterion. The initiation debonding angle either corresponds to an arrest debonding angle or is followed by unstable crack propagation up to the arrest debonding angle depending on the material tensile and shear strengths and opening and shear critical ERR. Restricting the simulated arrest debonding angles to the range measured experimentally enables determining a range of admissible interface critical ERR and tensile and shear strengths. An optimum set of parameters is finally determined by confrontation of the debonding angle variation as a function of the applied stress. A perspective to this work will consist in improving the proposed approach by considering 3D models and observations of the fiber-matrix debonding process.

References

[1] S.-J. Park, M.-K. Seo, J.-R. Lee, Roles of interfaces between carbon fibers and epoxy matrix on interlaminar fracture toughness of composites, Composite Interfaces 13 (2-3) (2006) 249–267, publisher: Taylor & Francis. doi:10.1163/156855406775997079.
URL https://doi.org/10.1163/156855406775997079

[2] A. C. Johnson, S. A. Hayes, F. R. Jones, The role of matrix cracks and fibre/matrix debonding on the stress transfer between fibre and matrix in a single fibre fragmentation test, Composites Part A: Applied Science and Manufacturing 43 (1) (2012) 65–72. doi:10.1016/j.compositesa.2011.09.005.
URL https://www.sciencedirect.com/science/article/pii/S1359835X11002892

[3] H. Dève, S. Schmauder, Role of interface properties on the toughness of brittle matrix composites reinforced with ductile fibers, Journal of Materials Research 7 (11) (1992) 3132–3138, edition: 2011/01/31 Publisher: Cambridge University Press. doi:10.1557/JMR.1992.3132.
URL https://www.cambridge.org/core/article/role-of-interface-properties-on-the-toughness-of-brittle-matrix-composites-reinforced-with-ductile-fibers/1A898FDEA6E62E1BAEF57E04CA47FC19

[4] D. Tripathi, F. R. Jones, Single fibre fragmentation test for assessing adhesion in fibre reinforced composites, Journal of Materials Science 33 (1) (1998) 1–16. doi:10.1023/A:1004351606897.
URL https://doi.org/10.1023/A:1004351606897

[5] C. V. Singh, R. Talreja, Damage in composite materials, in: Damage and Failure of Composite Materials, Cambridge University Press, Cambridge, 2012, pp. 36–56. doi:10.1017/CBO9781139016063.004.
URL https://www.cambridge.org/core/books/damage-and-failure-of-composite-materials/damage-in-composite-materials/79913CFC3E07B24C0A9CBBECC0B96510

[6] P. Herrera-Franco, L. Drzal, Comparison of methods for the measurement of fibre/matrix adhesion in composites, Composites 23 (1) (1992) 2–27. doi:10.1016/0010-4361(92)90282-Y.
URL https://www.sciencedirect.com/science/article/pii/001043619290282Y

[7] S. Zhandarov, E. Mäder, Characterization of fiber/matrix interface strength: applicability of different tests, approaches and parameters, Composites Science and Technology 65 (1) (2005) 149–160. doi:10.1016/j.compscitech.2004.07.003.
URL https://www.sciencedirect.com/science/article/pii/S026635380400171X

[8] L. Yang, J. Thomason, Interface strength in glass fibre–polypropylene measured using the fibre pull-out and microbond methods, Special Issue on 10th Deformation & Fracture of Composites Conference: Interfacial interactions in composites and other applications 41 (9) (2010) 1077–1083. doi:10.1016/j.compositesa.2009.10.005.
URL https://www.sciencedirect.com/science/article/pii/S1359835X09003157

[9] M. Nishikawa, T. Okabe, N. Takeda, Determination of interface properties from experiments on the fragmentation process in single-fiber composites, Materials Science and Engineering: A 480 (1) (2008) 549–557. doi:10.1016/j.msea.2007.07.067.
URL https://www.sciencedirect.com/science/article/pii/S0921509307014797

[10] J. Mandell, J. Chen, F. McGarry, A microdebonding test for in situ assessment of fibre/matrix bond strength in composite materials, International Journal of Adhesion and Adhesives 1 (1) (1980) 40–44. doi:10.1016/0143-7496(80)90033-0.
URL https://www.sciencedirect.com/science/article/pii/0143749680900330

[11] B. Miller, P. Muri, L. Rebenfeld, A microbond method for determination of the shear strength of a fiber/resin interface, Composites Science and Technology 28 (1) (1987) 17–32. doi:10.1016/0266-3538(87)90059-5.
URL https://www.sciencedirect.com/science/article/pii/0266353887900595

[12] L. J. Broutman, Glass-resin joint strength and their effect on failure mechanisms in reinforced plastics, Polymer Engineering and Science 6 (3) (1966) 263–272, publisher: Wiley. doi:10.1002/pen.760060316.
URL https://doi.org/10.1002/pen.760060316

[13] C. Ageorges, K. Friedrich, T. Schüller, B. Lauke, Single-fibre Broutman test: fibre–matrix interface transverse debonding, Composites Part A: Applied Science and Manufacturing 30 (12) (1999) 1423–1434. doi:10.1016/S1359-835X(99)00045-7.
URL https://www.sciencedirect.com/science/article/pii/S1359835X99000457

[14] D. Gundel, B. Majumdar, D. Miracle, Evaluation of the transverse response of fiber-reinforced composites using a cross-shaped sample geometry, Scripta Metallurgica et Materialia 33 (12) (1995) 2057–2065. doi:10.1016/0956-716X(95)00459-9.
URL https://www.sciencedirect.com/science/article/pii/0956716X95004599

[15] V. T. Bechel, G. P. Tandon, Characterization of interfacial failure using a reflected light technique, Experimental Mechanics 42 (2) (2002) 200–205. doi:10.1007/BF02410884.
URL https://doi.org/10.1007/BF02410884

[16] G. Tandon, R. Kim, V. Bechel, Evaluation of interfacial normal strength in a SCS-0/epoxy composite with cruciform specimens, Composites Science and Technology 60 (12) (2000) 2281–2295. doi:10.1016/S0266-3538(00)00020-8.
URL https://www.sciencedirect.com/science/article/pii/S0266353800000208

[17] J. Koyanagi, P. D. Shah, S. Kimura, S. K. Ha, H. Kawada, Mixed-mode interfacial debonding simulation in single-fiber composite under a transverse load, Journal of Solid Mechanics and Materials Engineering 3 (5) (2009) 796–806. doi:10.1299/jmmp.3.796.

[18] K. Martyniuk, B. F. Sørensen, P. Modregger, E. M. Lauridsen, 3D in situ observations of glass fibre/matrix interfacial debonding, Composites Part A: Applied Science and Manufacturing 55 (2013) 63–73. doi:10.1016/j.compositesa.2013.07.012.
URL https://www.sciencedirect.com/science/article/pii/S1359835X13001966

[19] C. Montgomery, B. Koohbor, N. Sottos, A Robust Patterning Technique for Electron Microscopy-Based Digital Image Correlation at Sub-Micron Resolutions, Experimental Mechanics 59 (7) (2019) 1063–1073. doi:10.1007/s11340-019-00487-2.
URL https://doi.org/10.1007/s11340-019-00487-2

[20] R. Livingston, B. Koohbor, Characterizing fiber-matrix debond and fiber interaction mechanisms by full-field measurements, Composites Part C: Open Access 7 (2022) 100229. doi:10.1016/j.jcomc.2022.100229.
URL https://www.sciencedirect.com/science/article/pii/S2666682022000020

[21] E. Martin, D. Leguillon, A. Catapano, N. Carrère, Prediction of interfacial debonding between stiff spherical particles and a soft matrix with the coupled criterion, Theoretical and Applied Fracture Mechanics 109 (2020) 102749. doi:10.1016/j.tafmec.2020.102749.
URL https://www.sciencedirect.com/science/article/pii/S0167844220303256

[22] T. Gentieu, J. Jumel, A. Catapano, J. Broughton, Size effect in particle debonding: Comparisons between finite fracture mechanics and cohesive zone model, Journal of Composite Materials 53 (14) (2019) 1941–1954, publisher: SAGE Publications Ltd STM. doi:10.1177/0021998318816471.
URL https://doi.org/10.1177/0021998318816471

[23] V. Kushch, S. Shmegera, P. Brøndsted, L. Mishnaevsky, Numerical simulation of progressive debonding in fiber reinforced composite under transverse loading, Recent Advances in Micromechanics of Materials 49 (1) (2011) 17–29. doi:10.1016/j.ijengsci.2010.06.020.
URL https://www.sciencedirect.com/science/article/pii/S0020722510001278

[24] I. García, V. Mantič, E. Graciani, Debonding at the fibre–matrix interface under remote transverse tension. One debond or two symmetric debonds?, European Journal of Mechanics - A/Solids 53 (2015) 75–88. doi:10.1016/j.euromechsol.2015.02.007.
URL https://www.sciencedirect.com/science/article/pii/S0997753815000200

[25] V. Mantič, I. García, Crack onset and growth at the fibre–matrix interface under a remote biaxial transverse load. Application of a coupled stress and energy criterion, International Journal of Solids and Structures 49 (17) (2012) 2273–2290. doi:10.1016/j.ijsolstr.2012.04.023.
URL https://www.sciencedirect.com/science/article/pii/S0020768312001709

[26] M. Muñoz-Reja, L. Távara, V. Mantič, P. Cornetti, Influence of a neighbour fibre on the onset and growth of a fibre-matrix debond under biaxial loading. A study by Finite Fracture Mechanics at linear elastic interfaces, 21st European Conference on Fracture, ECF21, 20-24 June 2016, Catania, Italy 2 (2016) 2022–2029. doi:10.1016/j.prostr.2016.06.254.
URL https://www.sciencedirect.com/science/article/pii/S2452321616302657

[27] C. Sandino, E. Correa, F. París, Numerical analysis of the influence of a nearby fibre on the interface crack growth in composites under transverse tensile load, Modeling of fracture and damage in composite materials 168 (2016) 58–75. doi:10.1016/j.engfracmech.2016.01.022.
URL https://www.sciencedirect.com/science/article/pii/S0013794416000503

[28] M. Velasco, E. Correa, F. París, Interaction between fibres in the transverse damage in composites, Engineering Fracture Mechanics 239 (2020) 107273. doi:10.1016/j.engfracmech.2020.107273.
URL https://www.sciencedirect.com/science/article/pii/S0013794420308560

[29] P. Cornetti, A. Sapora, A. Carpinteri, Short cracks and V-notches: Finite Fracture Mechanics vs. Cohesive Crack Model, Modeling of fracture and damage in composite materials 168 (2016) 2–12. doi:10.1016/j.engfracmech.2015.12.016.
URL https://www.sciencedirect.com/science/article/pii/S0013794415006906

[30] A. Doitrand, C. Fagiano, F. Hild, V. Chiaruttini, A. Mavel, M. Hirsekorn, Mesoscale analysis of damage growth in woven composites, Composites Part A: Applied Science and Manufacturing 96 (2017) 77–88. doi:10.1016/j.compositesa.2017.02.018.
URL https://www.sciencedirect.com/science/article/pii/S1359835X17300660

[31] V. Mantič, Interface crack onset at a circular cylindrical inclusion under a remote transverse tension. Application of a coupled stress and energy criterion, International Journal of Solids and Structures 46 (6) (2009) 1287–1304. doi:10.1016/j.ijsolstr.2008.10.036.
URL https://www.sciencedirect.com/science/article/pii/S0020768308004630

[32] D. Leguillon, Strength or toughness? A criterion for crack onset at a notch, European Journal of Mechanics - A/Solids 21 (1) (2002) 61–72. doi:https://doi.org/10.1016/S0997-7538(01)01184-6.
URL https://www.sciencedirect.com/science/article/pii/S0997753801011846

[33] Z. Tomičević, S. Roux, F. Hild, Evaluation of fatigue crack network growth in cast iron for different biaxial loading paths via full-field measurements, International Journal of Fatigue 92 (2016) 281–303. doi:10.1016/j.ijfatigue.2016.07.013.
URL https://www.sciencedirect.com/science/article/pii/S0142112316302171

[34] A. Doitrand, R. Henry, H. Saad, S. Deville, S. Meille, Determination of interface fracture properties by micro- and macro-scale experiments in nacre-like alumina, Journal of the Mechanics and Physics of Solids 145 (2020) 104143. doi:10.1016/j.jmps.2020.104143.
URL https://www.sciencedirect.com/science/article/pii/S002250962030377X

[35] J. Hutchinson, Z. Suo, Mixed Mode Cracking in Layered Materials, in: J. W. Hutchinson, T. Y. Wu (Eds.), Advances in Applied Mechanics, Vol. 29, Elsevier, 1991, pp. 63–191. doi:10.1016/S0065-2156(08)70164-9.
URL https://www.sciencedirect.com/science/article/pii/S0065215608701649

[36] A. Doitrand, E. Martin, D. Leguillon, Numerical implementation of the coupled criterion: Matched asymptotic and full finite element approaches, Finite Elements in Analysis and Design 168 (2020) 103344. doi:10.1016/j.finel.2019.103344.
URL https://www.sciencedirect.com/science/article/pii/S0168874X19303002

[37] E. Martin, T. Vandellos, D. Leguillon, N. Carrère, Initiation of edge debonding: coupled criterion versus cohesive zone model, International Journal of Fracture 199 (2) (2016) 157–168. doi:10.1007/s10704-016-0101-2.
URL https://doi.org/10.1007/s10704-016-0101-2

[38] E. Martin, D. Leguillon, O. Sevecek, R. Bermejo, Understanding the tensile strength of ceramics in the presence of small critical flaws, Engineering Fracture Mechanics 201 (2018) 167–175. doi:10.1016/j.engfracmech.2018.06.021.
URL https://www.sciencedirect.com/science/article/pii/S0013794418303837

[39] S. Ogihara, Y. Sakamoto, J. Koyanagi, Evaluation of Interfacial Tensile Strength in Glass Fiber/Epoxy Resin Interface using the Cruciform Specimen Method, Journal of Solid Mechanics and Materials Engineering 3 (9) (2009) 1071–1080. doi:10.1299/jmmp.3.1071.

[40] J. Varna, L. Berglund, M. Ericson, Transverse single-fibre test for interfacial debonding in composites: 2. Modelling, Composites Part A: Applied Science and Manufacturing 28 (4) (1997) 317–326. doi:10.1016/S1359-835X(96)00125-X.
URL https://www.sciencedirect.com/science/article/pii/S1359835X9600125X

[41] K. R. Totten, B. Kutub, L. A. Carlsson, In situ determination of the fiber–matrix interface tensile strength, Journal of Composite Materials 50 (5) (2016) 589–599, publisher: SAGE Publications Ltd STM. doi:10.1177/0021998315579926.
URL https://doi.org/10.1177/0021998315579926

[42] N. Chandra, Evaluation of interfacial fracture toughness using cohesive zone model, Composites Part A: Applied Science and Manufacturing 33 (10) (2002) 1433–1447. doi:10.1016/S1359-835X(02)00173-2.
URL https://www.sciencedirect.com/science/article/pii/S1359835X02001732

[43] N. Taniguchi, K. Toge, H. Kawada, Evaluation of the mechanical properties of PMC interface using slice compression test — Analysis of transfer mechanism of interfacial shear stress, Composite Interfaces 7 (5-6) (2000) 349–361, publisher: Taylor & Francis. doi:10.1163/156855400750262879.
URL https://doi.org/10.1163/156855400750262879

[44] A. Doitrand, D. Leguillon, E. Martin, Computation of generalized stress intensity factors of 3D singularities, International Journal of Solids and Structures 190 (2020) 271–280. doi:10.1016/j.ijsolstr.2019.11.019.
URL https://www.sciencedirect.com/science/article/pii/S0020768319304792

[45] A. Doitrand, D. Leguillon, Comparison between 2D and 3D applications of the coupled criterion to crack initiation prediction in scarf adhesive joints, International Journal of Adhesion and Adhesives 85 (2018) 69–76. doi:10.1016/j.ijadhadh.2018.05.022.
URL https://www.sciencedirect.com/science/article/pii/S0143749618301416